Detecting the Onset of Strain Localisation using Two-dimensional Wavelet Analysis on Sandstone Deformed at Different Effective Pressures

Roberto G. Rizzo, David Healy, Michael Heap, Natalie Farrell

AGU100 ADVANCING EARTH AND SPACE SCIENCE

JGR

Journal of Geophysical Research: Solid Earth

RESEARCH ARTICLE
10.1029/2018JB015898

Key Points:
- The 2-D Morlet wavelet analysis detected variations in the onset of strain localization for experiments performed at different effective pressures
- Two distinct critical crack lengths were detected for increasing effective pressures, indicating different shear failure initiation modes
- The 2-D Morlet wavelet analysis of thin sections provided quantitative data on the processes of strain localization in the brittle field

Supporting Information:
- Supporting Information S1

Correspondence to:
R. E. Rizzo,
rerizzo@abdn.ac.uk

Citation:
Rizzo, R. E., Healy, D., Heap, M. J., & Farrell, N. J. (2018). Detecting the onset of strain localization using two-dimensional wavelet analysis on sandstone deformed at different effective pressures. *Journal of Geophysical Research: Solid Earth*, *123*, 10,460–10,478. https://doi.org/10.1029/2018JB015898

Received 3 APR 2018
Accepted 26 NOV 2018
Accepted article online 28 NOV 2018
Published online 21 DEC 2018

Detecting the Onset of Strain Localization Using Two-Dimensional Wavelet Analysis on Sandstone Deformed at Different Effective Pressures

Roberto E. Rizzo[1,2], David Healy[1], Michael J. Heap[3], and Natalie J. Farrell[1]

[1]School of Geosciences, King's College, University of Aberdeen, Aberdeen, UK, [2]School of Materials, University of Manchester at Research Complex at Harwell, Rutherford Appleton Laboratory, Oxfordshire, UK, [3]Géophysique Expérimentale, Institut de Physique du Globe de Strasbourg (UMR 7516 CNRS, Université de Strasbourg/EOST), 5 rue René Descartes, Strasbourg, France

Abstract Laboratory brittle deformation experiments have shown that a rapid transition exists in the behavior of porous materials under stress: At a certain point, early formed and spatially distributed tensile cracks interact and coalesce forming a shear plane. In this work, we present and apply a novel image processing tool that is able to quantify this transition between distributed ("stable") damage accumulation and localized ("unstable") deformation, in terms of the size, density, and orientation of cracks at the point of strain localization. Our technique, based on a two-dimensional Morlet wavelet analysis, can recognize, extract, and visually separate the multiscale changes occurring in the crack network during the deformation process. We first performed a series of triaxial experiments ($\sigma_1 > \sigma_2 = \sigma_3$) on core plugs of Hopeman Sandstone (Scotland, UK) at different effective pressures (from 5 to 30 MPa). We then processed high-resolution backscattered electron microscope images of thin sections of these core plugs and found differences in the strain localization process as effective pressure was increased. The critical length of tensile cracks required before the onset of strain localization was reduced from 0.24 to 0.15 mm as the effective pressure was increased to 30 MPa, resulting in a narrow fracture zone. Critically, by comparing patterns of fractures in these deformed sandstone samples, we can quantitatively explore the relationship between the observed geometry of the cracks and the inferred mechanical processes. This will eventually help us to better understand the physics underlying the initiation of catastrophic events, such as earthquakes, landslides, and volcanic eruptions.

1. Introduction

Understanding the rupture process of initially intact rocks is a basic aim of experimental rock deformation in the brittle field. The propagation of a shear plane (i.e., a fault) by a mechanism of en-echelon tensile crack coalescence has been proposed from field evidence (e.g., Jourde et al., 2002; McGrath & Davison, 1995), from experimental evidence (e.g., Lockner et al., 1991; Petit & Barquins, 1988; Stanchits et al., 2006), and from theoretical and numerical modeling (e.g., Healy et al., 2006a, 2006b; Reches & Lockner, 1994). It is generally accepted that shearing becomes the dominant mechanism when *sufficient* tensile damage has been generated. The location of acoustic emission (AE) events, related to microcrack generation throughout the loading cycle (Lockner et al., 1992; Lockner, 1993; Moore & Lockner, 1995), enables the mapping of microcrack formation prior to bulk—that is, whole sample—failure, showing that a fault initiates by the interaction of cracks even at relatively low *average crack density*. However, in the field of rock mechanics, a quantitative mapping of the proportion of cracks whereat tensile fracturing gives way to a throughgoing shear fracture has rarely been performed. It has been recognized (e.g., Reches & Lockner, 1994) that the interaction starts by dilatation of one or more cracks that induces dilatation of certain neighboring cracks that were themselves on the verge of opening, in an overall process that involves coalescence of tensile cracks, grain-boundary cracks, and porosity (Dunn et al., 1973). However, this effect of self-organized "contamination," which ultimately leads the rock to bulk shear failure, requires the existence of a minimum distance among contiguous en-echelon tensile cracks—that is, a critical density, an interflaw length (Vasseur et al., 2017)—together with a certain minimum

size of cracks—that is, a critical crack length. In this paper, we specifically address these two questions:

1. Is it now possible to quantitatively determine the point of transition in the length and/or density of microcracking during brittle deformation, to assess and constrain the magnitude of "sufficient tensile damage" in order for shear failure to initiate?
2. How much influence does the applied stress field (i.e., the effective pressure) have on the point of transition between tensile damage and shear failure?

Being able to characterize in a quantitative manner the abrupt changes in the interaction of tensile cracks and incipient faults is crucial to fully comprehend the mechanics of fault initiation, which has direct implications for earthquake nucleation and seismology, and rock-mass stability.

Image analysis techniques succeeded to identify petrographic and textural features—for example, mineral and grain clustering—on rock thin-sections (Reedy, 2006). More recently a number of automatic and semiautomatic algorithms have been developed for identifying cracked regions in composite artificial (e.g., concrete and steel; Yeum & Dyke, 2015) or natural materials (e.g., Arena et al., 2014; Voorn et al., 2013). All these methods employ segmentation procedures based on various object detection techniques such as Radon Transformation (Yeum & Dyke, 2015) and Hessian Filtering (Voorn et al., 2013). In a recent work Rizzo, Healy, Farrell, and Heap (2017) demonstrated the applicability of the Morlet wavelet analysis for detecting fracture size and orientation transitions during the deformation history of a rock sample. Here we extend the method to investigate and characterize the brittle deformation process of a low-medium porosity (11% on average) sandstone, deformed in a conventional triaxial (axisymmetric) deformation apparatus under different effective pressures. The analysis is based on postfailure fracture maps of high-resolution montages of backscattered electron (BSE) microscope images. These montages allow total coverage of the fractured area of the specimens, enabling us to map the crack and incipient-fault interactions for a suite of three samples deformed at progressively higher effective pressures. First, we present the results of the wavelet analysis for each sample. Second, from the derived optimum wavelet coefficient maps, we focus on the geometrical and kinematic attributes of crack/fault relationships to infer the critical lengths, which mark the transition between diffuse tensile cracking and localized shear failure. We demonstrate the ability of wavelet analysis to investigate the evolution through time of crack sizes and their spatial densities using postfailure static images. By comparing the different samples, the role of effective pressure on crack initiation and propagation is also assessed, and the relevance of these findings for interpreting the physical processes at the base of large scale rock failure is also considered.

The wavelet analysis technique presented in this work is part of the FracPaQ toolbox (Healy et al., 2017), which can be freely downloaded from https://github.com/DaveHealy-Aberdeen/FracPaQ. With the introduction of this new tool, FracPaQ now allows the user to perform a comprehensive analysis of fracture networks, in both their key "static"—for example, length distribution, spatial density and connectivity—and "dynamic" features—for example, variation in the hierarchy of cracks.

2. Materials and Methods

2.1. Sample Description and Setup for Laboratory Deformation Tests

We mapped microcracks from images of three centimeter-scale thin sections made from core plugs of the Hopeman Sandstone Formation, a Permian quartz arenite (Edwards et al., 1993; Farrell et al., 2014), taken to failure under triaxial conditions in the laboratory. Intact blocks were taken from the Clashach quarry on the coast of Moray (Scotland, UK), and cylindrical core plugs 20 mm in diameter and 40 mm long were prepared. This quartz-cemented arenite is texturally mature (>92% quartz grains and <8% K-feldspar and subordinate lithics) and well-sorted (optical microscopy showed that grains have a fine to medium grain size and mean grain diameter of 0.25–0.4 mm; Farrell & Healy, 2017). Samples were chosen based on homogeneity: without visible laminations and with uniform grain size, very similar porosity, and cement distribution. Three core plugs of Hopeman Sandstone were deformed in a conventional triaxial compressional apparatus ($\sigma_1 > \sigma_2 = \sigma_3$). The core plugs were first vacuum-saturated in deionized water. Following saturation, the samples were inserted into a rubber (viton) jacket and placed inside the triaxial deformation apparatus. The samples were then subjected to confining pressures (P_c) ranging between 15 and 40 MPa and a constant pore fluid (deionized water) pressure (P_f) of 10 MPa. These pressures were increased slowly (0.05 MPa/s) on the sample and such that the target effective pressure (P_{eff}; where $P_{eff} = P_c - \alpha P_f$; we assume here a simple effective

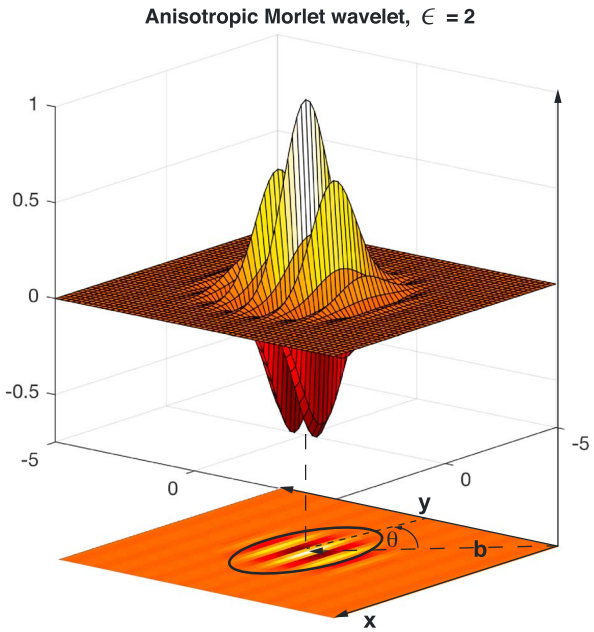

Figure 1. Two-dimensional anisotropic Morlet wavelet $\Psi(a, \mathbf{b}, \theta, \epsilon)$. Top image shows the wavelet in the spatial domain, seen in a 3-D perspective. The bottom image shows the wavelet represented as level curves; here the black ellipse is the envelope (i.e., the wavelet "footprint") that contains most of the energy of the wavelet. Representations of the location parameter (**b**) and of the orientation parameter (θ) are also viewed in the Cartesian coordinates (x, y).

pressure law where $\alpha = 1$) was never exceeded. The confining and pore pressures were kept constant using servo-controlled pumps. The samples were left overnight under the target pressures to ensure microstructural equilibration. The samples were then loaded axially to failure at a constant strain rate of $10^{-5}s^{-1}$. Based on the high permeability of Hopeman sandstone ($\sim 5 \times 10^{-13}m^2$; Farrell et al., 2014), we expect our samples to be drained at a strain rate of $10^{-5}s^{-1}$ (see Heap & Wadsworth, 2016). During deformation we monitored axial force (using a load cell) and axial displacement (using a linear variable differential transducer located outside the pressure vessel), pore volume change (via the servo-controlled pore pressure pumps), and the output of AE energy. Axial force, axial displacement, and pore volume change were converted to axial stress, axial strain, and porosity change using the sample dimensions. AEs–high-frequency elastic wave packets generated by the rapid release of strain energy such as during microcracking—were recorded using a piezo-electric crystal attached to the top of the upper piston (see Farquharson et al., 2017, for a schematic diagram) and a single-channel AE recording system (Physical Acoustics AE Node) set at a threshold of 40 dB. AE energy is taken here as the area under the received waveform (and is therefore in arbitrary units).

Following deformation, the samples were carefully unloaded at a constant strain rate of $10^{-5}s^{-1}$ to avoid additional microcrack damage during unloading. The confining and pore pressures were then decreased slowly (0.05 MPa/s), such that the maximum effective pressure was never exceeded. Samples were Epoxy filled under a vacuum then thin sections were cut in the *XZ* plane of each core plug, that is, orthogonal to the strike of the throughgoing shear plane. The thin sections were hand ground thus minimizing the chance of grain plucking or fracturing induced during machine grinding. Montages of high-resolution (225 pixels per millimeter) BSE images taken at a magnification of ×100 from each thin section were taken on a FEI Quanta 200F environmental SEM at the University of Glasgow (UK). BSE images are very practical for microscale crack and pore mapping, because different minerals are represented with different grey levels and black represents void space, that is, pores and fractures (Farrell et al., 2014; Farrell & Healy, 2017; Griffiths et al., 2017; Wibberley et al., 2000). Fracture maps were produced by manually tracing all the visible cracks over the of the BSE mosaic using a vector graphic editor (Adobe Illustrator™). A number of automatic and semiautomatic algorithms for the segmentation of crack patterns have been recently developed (e.g., Arena et al., 2014; Delle Piane et al., 2015; Griffiths et al., 2017) and successfully used to isolate crack patterns in crystalline rocks with low primary porosity (e.g., granite and marble). However, these softwares become less accurate when analyzing rocks with more complex microstructures (i.e., sandstones; Griffiths et al., 2017). Therefore, although we recognize that subjectivity issues exist, we still prefer manually retracing the cracks: In this way the user is able to discern and identify specific features, discriminating cracks from pores, grain margins, and artifacts. Once produced, the fracture maps were converted into binary images; the resulting images were embedded in a white square matrix to avoid edge effects during the wavelet analysis (Ouillon et al., 1995).

2.2. Two-dimensional Continuous Wavelet Analysis for the Quantification of Multiscale Fracture Patterns

The spatial distribution of crack lengths and densities depend on, and vary with, the scale of analysis: They are multiscale properties (Gaillot et al., 1999; Ouillon et al., 1995, 1996). Consequently, for studying fracture trace maps, we need a tool that is able to efficiently perform a multiscale analysis of two-dimensional binary images. Wavelet analysis has emerged as a very powerful tool for signals (i.e., images) in which different scales are combined (Antoine et al., 1993). The method is based on projecting (convolving) the analyzed signal onto a family of elementary functions (filters), obtained by translating and dilating a single basic function, the analyzing wavelet (Ψ) (Figure 1). We based our study on a combination of the fully anisotropic directional Morlet wavelet algorithm of Neupauer and Powell (2005) and the wavelet coefficient method developed by Darrozes et al. (1997). This combination enables sharp unequivocal detection and quantification of any organized feature in a binary image, regardless of its scale, orientation, and location.

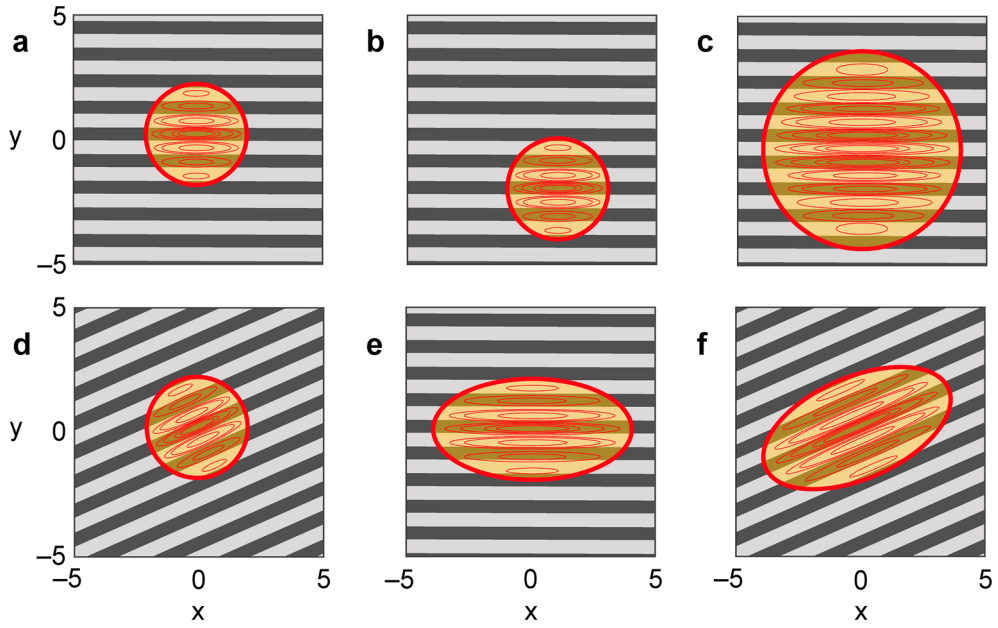

Figure 2. Example of continuous wavelet transform for a Morlet wavelet (modified after Neupauer & Powell, 2005). (a) Mother wavelet, (b) shifted wavelet (**b** = (1, −2)), (c) dilated wavelet ($a = 2$), (d) Rotated wavelet ($\theta = 110°$, counterclockwise with 0 parallel to *y*-axis), (e) anisotropic wavelet ($\epsilon = 2$), and (f) fully anisotropic wavelet ($\epsilon = 2$ and $\theta = 15°$). Red rings represent the envelope that contains most of the energy of the wavelet.

The anisotropic Morlet wavelet $\Psi(a, \mathbf{b}, \theta, \epsilon)$ is a function of four parameters that allows, for a given spatial resolution and a given position, the detection of structures in any direction (Figures 1 and 2): (1) the scale parameter (a), or resolution, allows multiscale analysis by dilatation/contraction of the wavelet; (2) the position vector (**b**) defines the location of the wavelet on the image and hence permits the filter to be moved over the whole field of the analyzed image; (3) the anisotropy parameter (ϵ) allows one to elongate the envelope of the wavelet (Figure 1) in the *x*-direction producing an elliptical "footprint" with a long axis in the *x*-direction, setting ϵ to unity we recover the isotropic wavelet; and (4) the orientation parameter (θ) permits the rotation of the wavelet for detecting any anisotropic feature (e.g., a fracture trace) in any direction (Figure 2). The Morlet wavelet is intrinsically directional, with peaks and troughs all aligned in one direction (Figure 1); when this wavelet is rotated through an angle θ the peaks and troughs are aligned along the direction of θ. In addition to being directional, the Morlet wavelet is also intrinsically anisotropic, meaning that it is elongated in the direction of θ (Neupauer & Powell, 2005).

The convolution, or wavelet transform (WT), of the image with each analyzing wavelet, obtained when we dilate/contract, elongate, rotate, and translate a mother wavelet (Ψ), produces a set of wavelet coefficients (WC), $W_\Psi(a, \mathbf{b}, \epsilon, \theta)$, which are local indicators of the quality of the match between the filter and the local content of the image (Gaillot et al., 2002, Figure 3). This set is called a wavelet image and is represented by a coefficient map (Figure 3). A constant signal would produce a null coefficient. Conversely, if the image shows "irregularities" (i.e., nonnull pixels), the wavelet reacts by producing nonnull coefficients. Small coefficients reflect a poor match between the given analyzing wavelet and the image; and maximum coefficients indicate optimal correlations between the filter and the content of the image under analysis. In practise, a complete and objective detection of all organized structures in a binary image requires the application of a range of filters each having a unique combination of the parameter triplets (a, ϵ, θ) values (Gaillot et al., 1997). Then the calculated coefficients $W_\Psi(a, \epsilon, \theta)$ at each point of the image are normalized with respect to the theoretical maximum value obtained for a perfect match between the wavelet and the analyzed structure. This normalization enhances the quality of the coefficient map—that is, produces an optimum map (Ouillon et al., 1995, Figure 3). In Figure 3 we show the basic procedure of wavelet transformation: For simplicity a synthetic fracture network is analyzed employing only two triplets (a, θ, ϵ) of the wavelet coefficients, two sizes, two orientations, and two anisotropy parameters. The different magnitudes of the coefficients for each resolution allow one to recognize the different level of organization of the image. The anisotropic Morlet wavelet

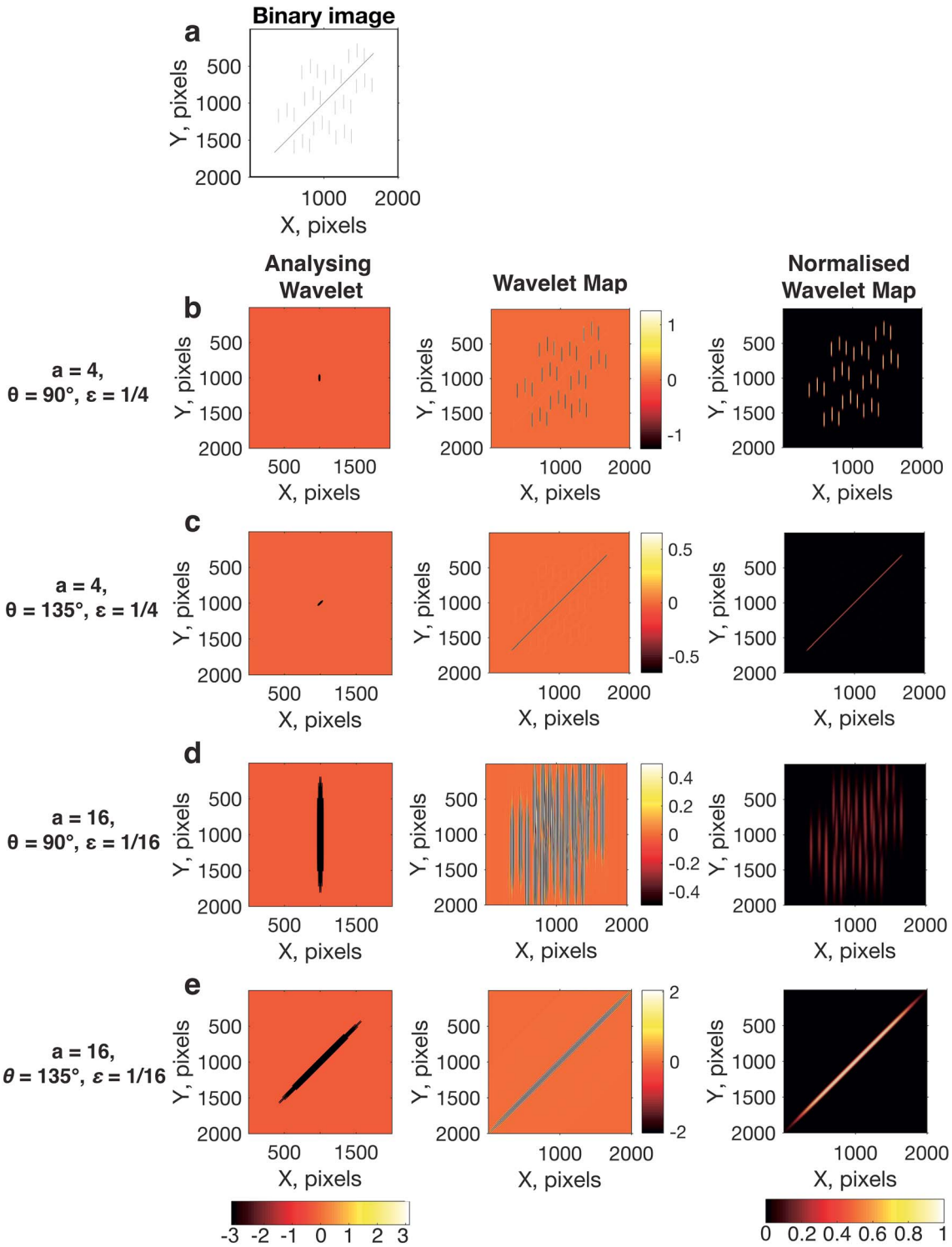

Figure 3. Wavelet analysis on a two-dimensional synthetic fracture network (a) composed of several vertical small cracks and one large inclined crack. (b–c) Analysis carried out with a small analyzing wavelet fixing the size ($a = 4$) and anisotropy ($\epsilon = 1/4$) while modifying the orientation parameter θ (90° in (b), and 135° in (c)). (d–e) Analysis obtained with a larger analyzing wavelet ($a = 16, \epsilon = 1/16$, while varying the orientation parameter θ). For each analysis (i.e., row), we show the analyzing anisotropic wavelet, the corresponding wavelet coefficient map before normalization and the normalized coefficient map, respectively. The use of a synthetic fracture pattern allows us to show the strong angular and dimensional selectivity of the anisotropic Morlet wavelet: Small and vertically oriented wavelet successfully catches the vertical small cracks (a), while a large wavelet is better suited to detect the long inclined fracture (d).

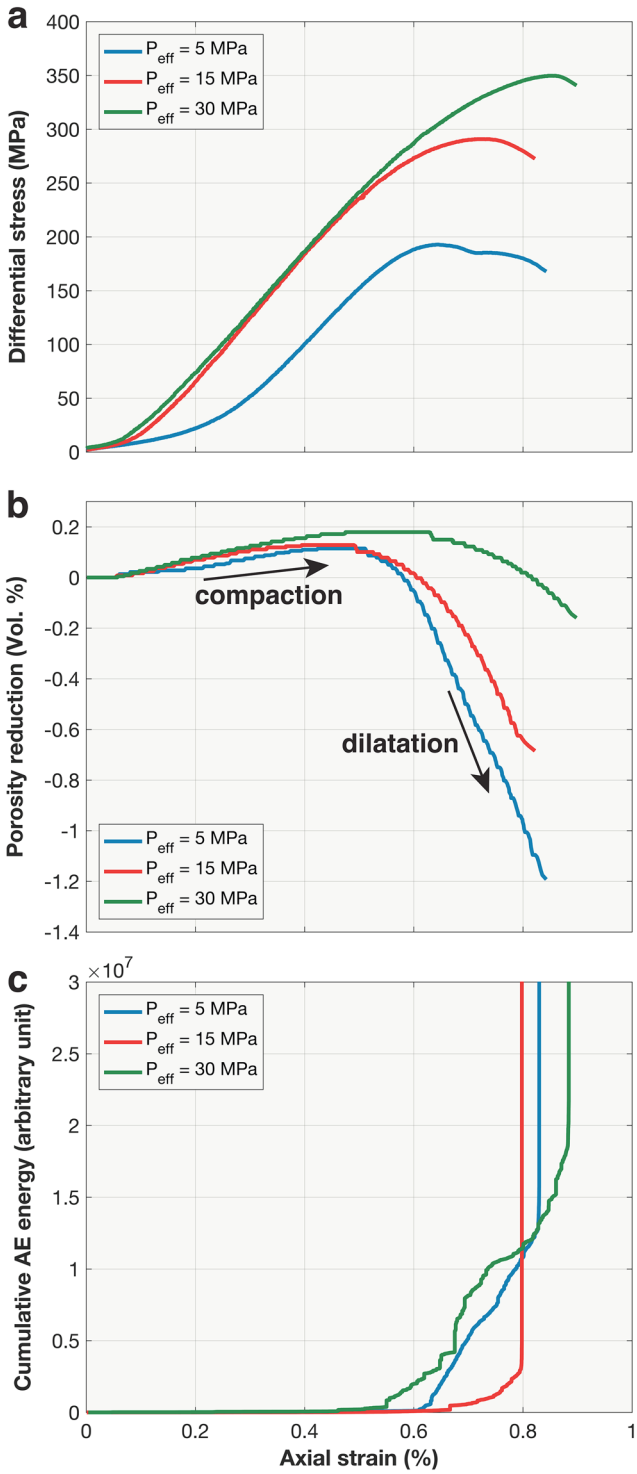

Figure 4. Hopeman Sandstone constant strain rate triaxial experiments. (a) Differential stress (MPa) as a function of axial strain for samples deformed at increasing effective pressures (5, 15, and 30 MPa). (b) The porosity reduction curves as a function of axial strain for the experiments shown in Figure 4a. (c) Cumulative acoustic emission energy (in arbitrary units) as function of axial strain for the experiments shown in Figure 4a.

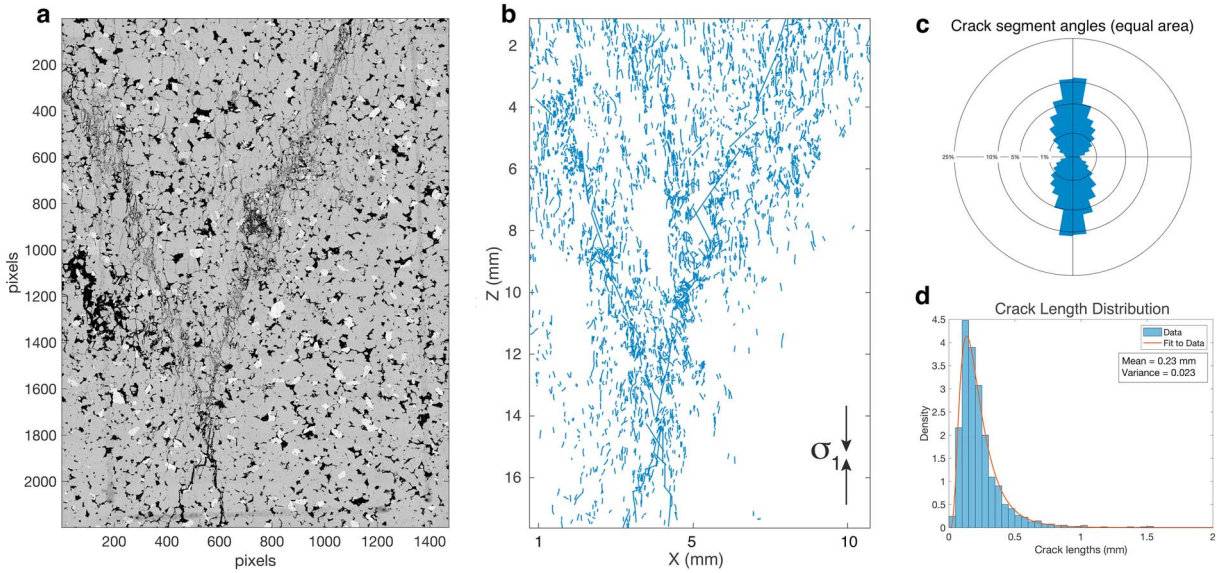

Figure 5. Fracture network in Sample 1. (a) Postfailure SEM-BSE high-resolution montage for Sample 1, deformed at P_{eff} = 5 MPa; σ_1 vertical. (b) Fracture map and (c) rose diagram (equal area) of all the fracture segments; the contribution of each crack segment to the frequency in each bin of the rose diagram is multiplied by its length (length weighted). (d) Histogram of length distribution of cracks, after removing lines relative to shear fractures. The best fit (red curve) is a log-normal distribution, derived from maximum likelihood analysis (MLE; Rizzo, Healy, & De Siena, 2017), with an arithmetic mean of 0.23 mm and variance of 0.023.

successfully quantifies the geometry of all features at a given scale *a*, whatever their location, shape anisotropy, and orientation.

Each optimum map is associated with optimum wavelets with known azimuths (θ); these azimuths correspond to the orientations of the detected structures in a known position **b**, at a given resolution (*a*). In our case, the detected structures in the images correspond to cracks formed during the deformation of the sandstone samples. From these azimuthal values, we can draw rose diagrams, which provide an overview of the variations in the cracks orientations with the scale of analysis. It follows that, if a sharp transition in the orientations of the crack traces is observed at a given scale (*a*), then this scale contains important information about the deformation process encapsulated in the crack pattern (Ouillon et al., 1995). When such a scale is detected, we perform a new analysis to determine its value with better accuracy.

The validity of the described method has been tested by Rizzo, Healy, Farrell, and Heap (2017) through the analysis of synthetic and natural fracture networks. This study found that the anisotropic Morlet wavelet performed better than its more commonly used counterpart, the Mexican hat wavelet, in the detection of oriented linear features, such as fracture traces, because of its inherent anisotropy. In addition, Rizzo, Healy, Farrell, and Heap (2017) described a complementary outcome that arose from the WC maps; from these maps, these authors directly retrieved information on the spatial density distribution of the analyzed features for a specific scale. Therefore, this type of analysis can provide insight into the processes of shear fracture growth from the interaction and coalescence of constituent tensile microcracks (Moore & Lockner, 1995). The analysis of Rizzo, Healy, Farrell, and Heap (2017) was however restricted to a single experiment. Here we use the wavelet analysis method to glean differences between the process of strain localization in sandstone samples deformed at different effective pressures.

3. Results

3.1. Mechanical Tests

The stress-strain curves for the three triaxial experiments on samples of Hopeman Sandstone are shown in Figure 3a. All three curves exhibit the classical stress-strain features of brittle rock in compression. Stress is first a nonlinearly increasing function of strain (Figure 4a), typically attributed to the closure of compliant pores/cracks (as evidenced by the porosity decrease shown in Figure 4b). This stage is followed by a quasi-linear elastic portion (Figure 4a). Following elastic deformation, the stress is a nonlinearly decreasing function (strain hardening) of strain prior to a peak stress (σ_p), typically attributed to the formation and growth

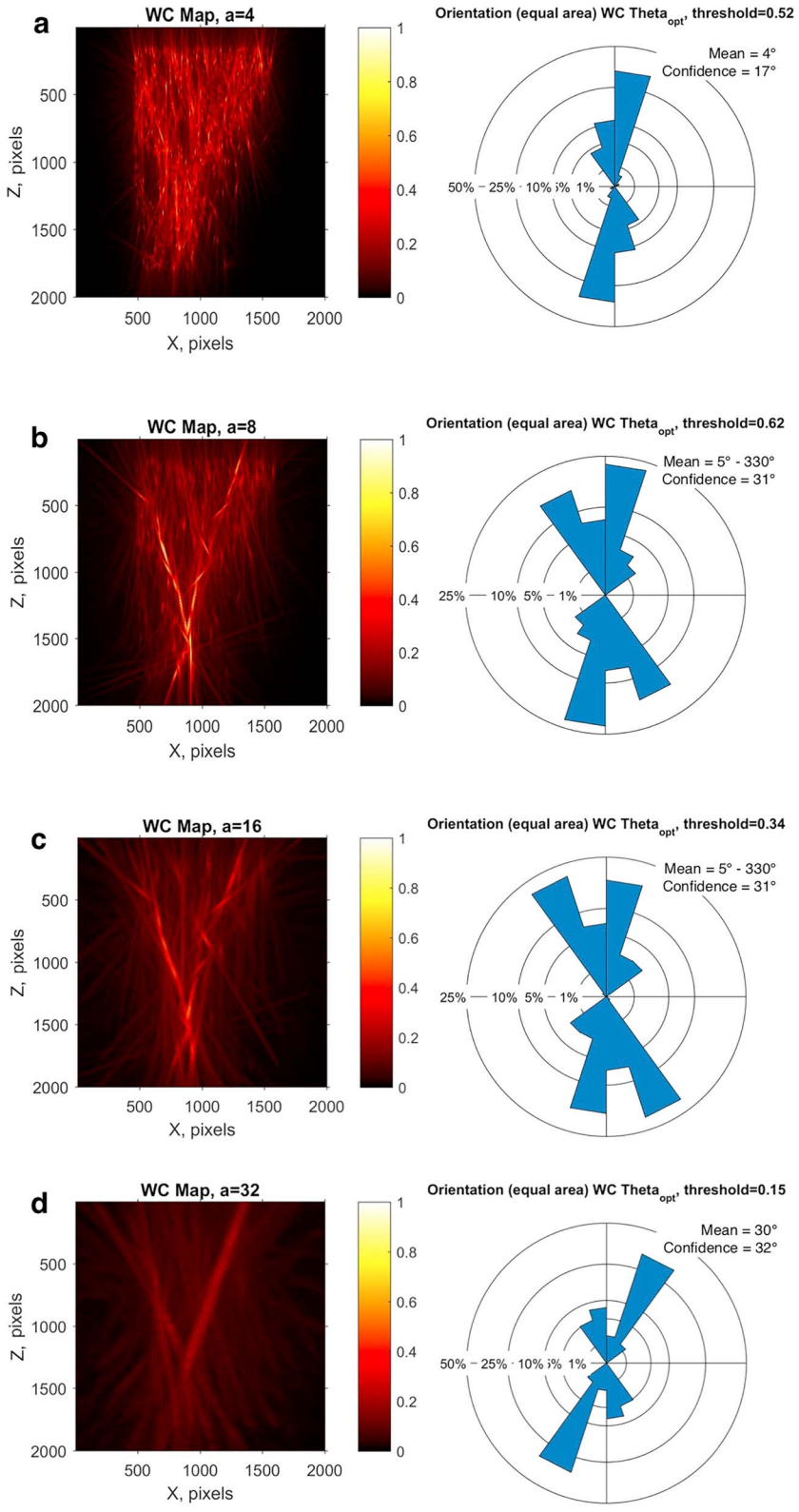

Figure 6. Morlet wavelet analysis applied to Sample 1 (P_{eff} = 5 MPa). The color scale shows the values of the normalized wavelet coefficients. Equal area rose diagrams of crack orientations are associated with wavelet coefficients (WCs) maps for each filter resolution. Inset text boxes contain descriptive statistics: circular mean vector azimuth (i.e., mean) and angular confidence interval. (a–d) Main orientation and size transitions in Sample 1 from early distributed tensile microcracks (a), the initiation of coalescence (b), to growth of two throughgoing shear planes (c–d); σ_1 vertical.

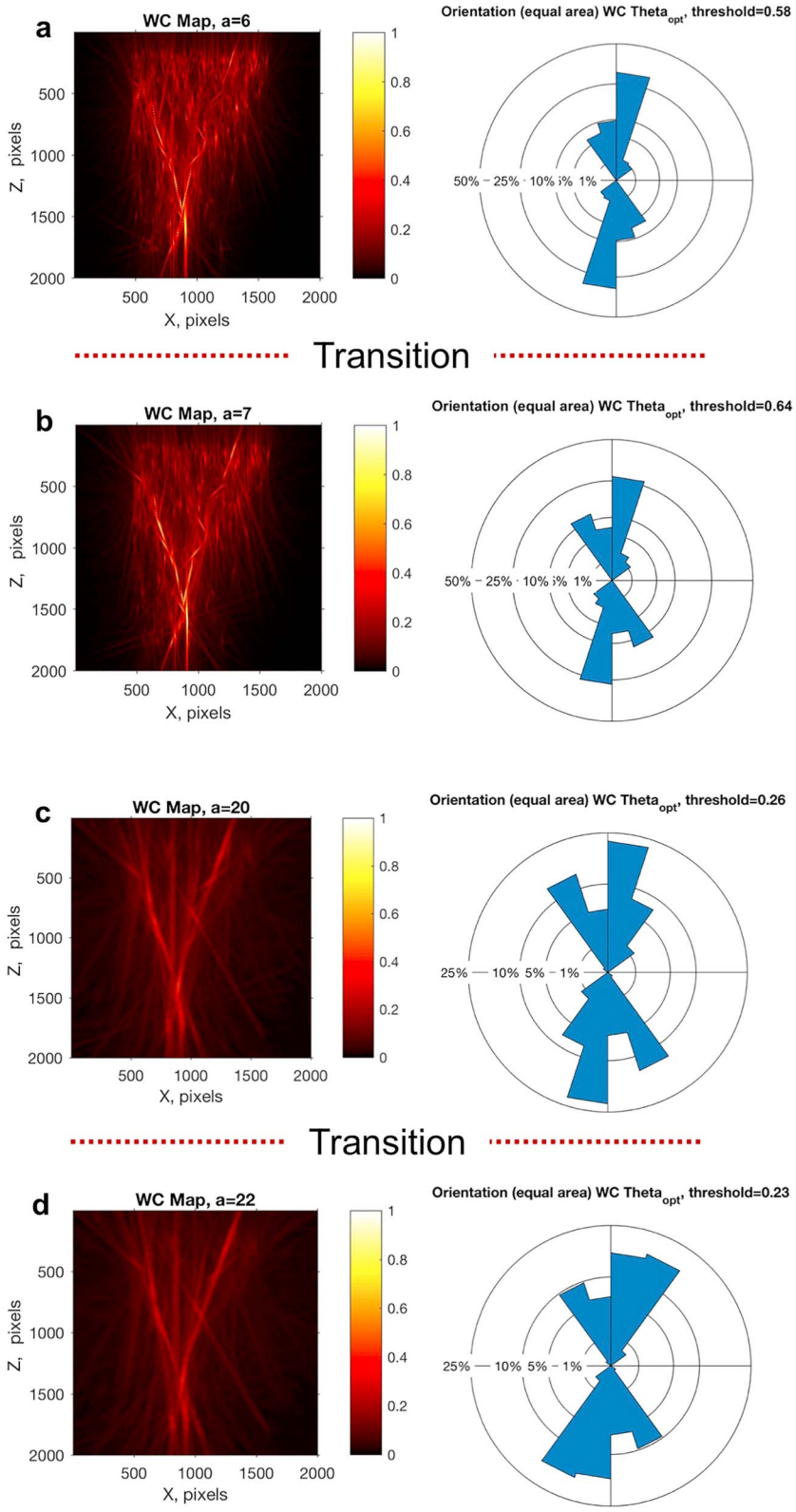

Figure 7. Identification of the precise orientation transitions for Sample 1. (a–b) The first transition has been detected between $a = 6$ and $a = 7$; this observation may correspond to clustering of initial tensile vertical cracks. (c–d) The second abrupt change in orientations has been imaged between $a = 20$ and $a = 22$; this stage may be associated with the evolution of a second and prominent shear plane.

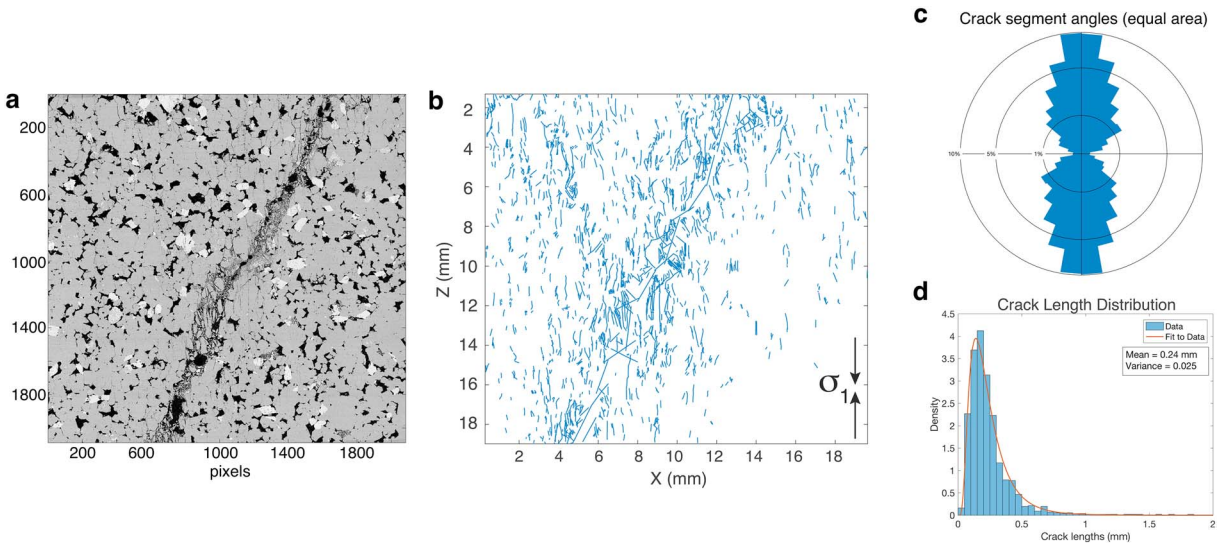

Figure 8. Fracture network in Sample 2. (a) Postfailure SEM-BSE high-resolution montage for Sample 2, deformed P_{eff} = 15 MPa; σ_1 vertical. (b) Fracture map and (c) rose diagram (equal area) of all the fracture segments. (d) Histogram of length distribution of cracks, after removing lines relative to shear fractures. The best fit (red curve) is a log-normal distribution, derived from MLE analysis, with an arithmetic mean of 0.24 mm and variance of 0.025.

of microcracks (as evidenced by the increase in porosity shown in Figure 4b and the appearance of AE activity shown in Figure 4c). The samples enter a strain-softening phase (a stress drop) following the peak stress (Figure 4a). The development of a shear fracture is often considered to occur during the strain-softening phase, which is characterized by large increases in porosity (Figure 4b) and significant AE activity (Figure 4c) (due to the growth and coalescence of microcracks). Visual inspection of our postmortem samples revealed the presence of shear fractures. The peak stress of Hopeman sandstone is higher at higher effective pressures: 192.8, 290.8, and 349.7 MPa at effective pressures of 5, 15, and 30 MPa, respectively (Figure 4a). These mechanical data are similar to those previously published on porous sandstones in the brittle regime (e.g., Baud et al., 2000; Klein et al., 2001; Menendez et al., 1996; Wong et al., 1997).

3.2. Morlet Wavelet Analysis

We applied wavelet processing to the set of fracture networks obtained from Hopeman Sandstone samples triaxially deformed at three different effective pressures (Figure 4). The inputs were digital, binary, fracture network maps, which mathematically can be described as a function $I(\mathbf{x})$ equal to 1 on pixels corresponding to fracture traces and equal to 0 otherwise. The convolution (or wavelet transform, WT) of $I(\mathbf{x})$ with the analyzing wavelets produces the optimum wavelet coefficients computed in the resulting wavelet maps. Because every resolution (a) and every anisotropy (ϵ) is explored, the preferred orientations of individual cracks and clusters of cracks can be extracted from the wavelet coefficient maps. Note that in the following descriptions, a high resolution (lower values of a) refers to short length scales, and low resolution (higher values of a) refers to longer length scales.

3.2.1. Low Effective Pressure—Sample 1

This sample was deformed at an effective pressure (P_{eff}) of 5 MPa (P_c = 15 MPa and P_f = 10 MPa) and failure occurred through the development of a conjugate set of shear planes (Figure 5a). The first wavelet coefficient to produce results is for a resolution a = 4 (Figure 6a); at this stage, we detect the presence of diffuse short cracks over about two thirds of the sample area (see Figures 5 and 6). These cracks are oriented parallel or subparallel to the applied maximum stress (σ_1). On incrementing the wavelet resolution to a = 8 (Figure 6b), while we observed that most cracks were still aligned parallel to the σ_1 (i.e., vertical), we noticed the appearance of a second prominent crack orientation oriented at an angle of 330° —that is, assuming that 0° is parallel to the z-axis. Thus, we identified a first oblique cluster of cracks, whose orientation will become predominant at a resolution of a = 16. This feature corresponded to the left inclined shear plane seen at failure in Sample 1. Finally, at the lowest resolution (a = 32) we recognized a second, now dominant, orientation at 30°, corresponding to the second shear plane on the sample. However, we also noted that a cluster of cracks with the same orientation was already detected for a = 8 (and consequently a = 16), although relatively minor.

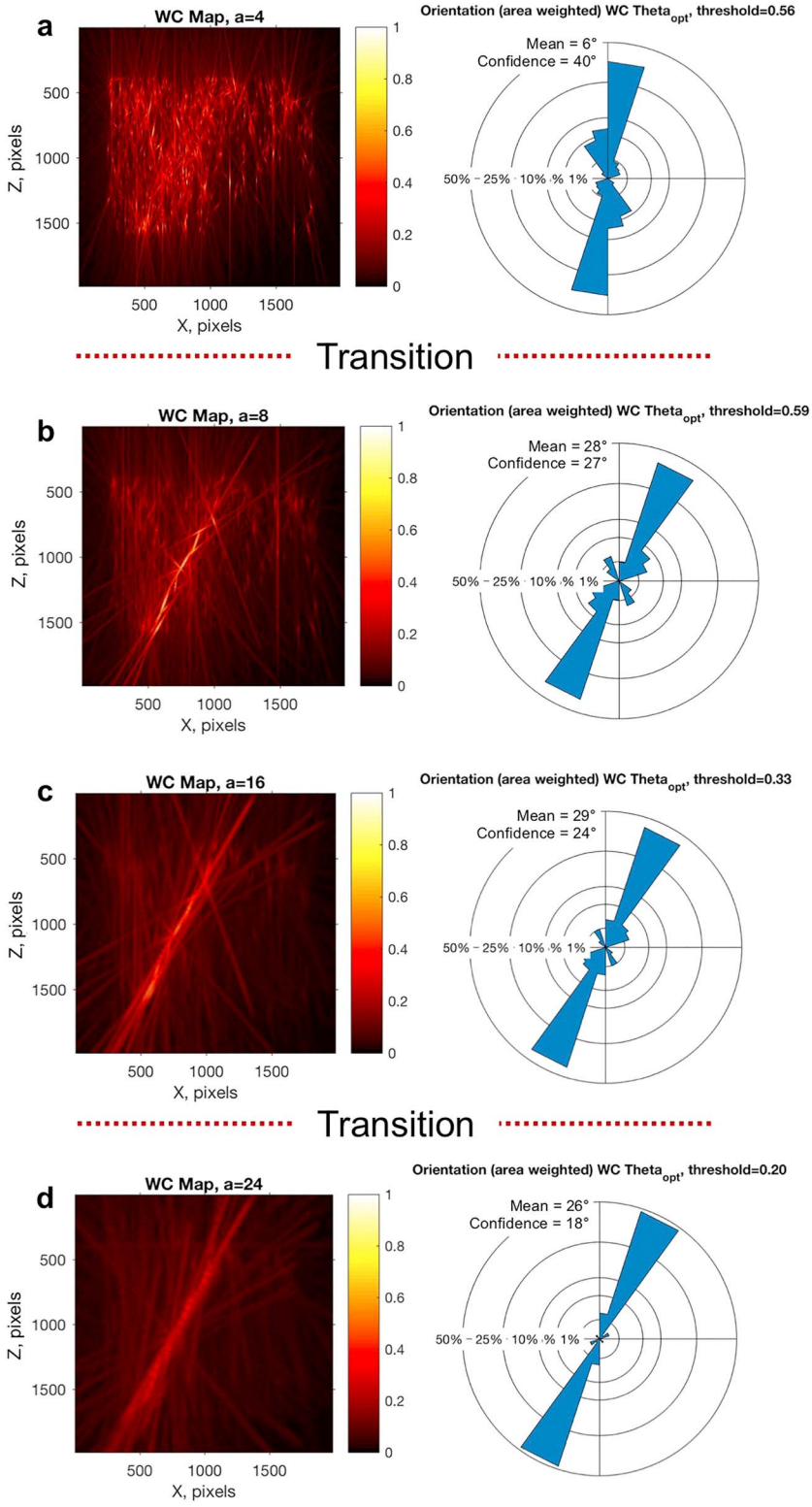

Figure 9. Morlet wavelet analysis applied to fracture network seen in Sample 2 (P_{eff} = 15 MPa). Color scale shows the values associated with normalized wavelet coefficients. Equal-area rose diagrams of fracture orientations correspond to wavelet coefficient (WC) maps at each filter resolution. Text boxes contain angular statistics: circular mean vector azimuth and angular confidence interval. (a–d) The orientation transitions from distributed microcracks (a) to localized scale fractures (b–d) are clearly captured with increasing size of the filter; σ_1 vertical.

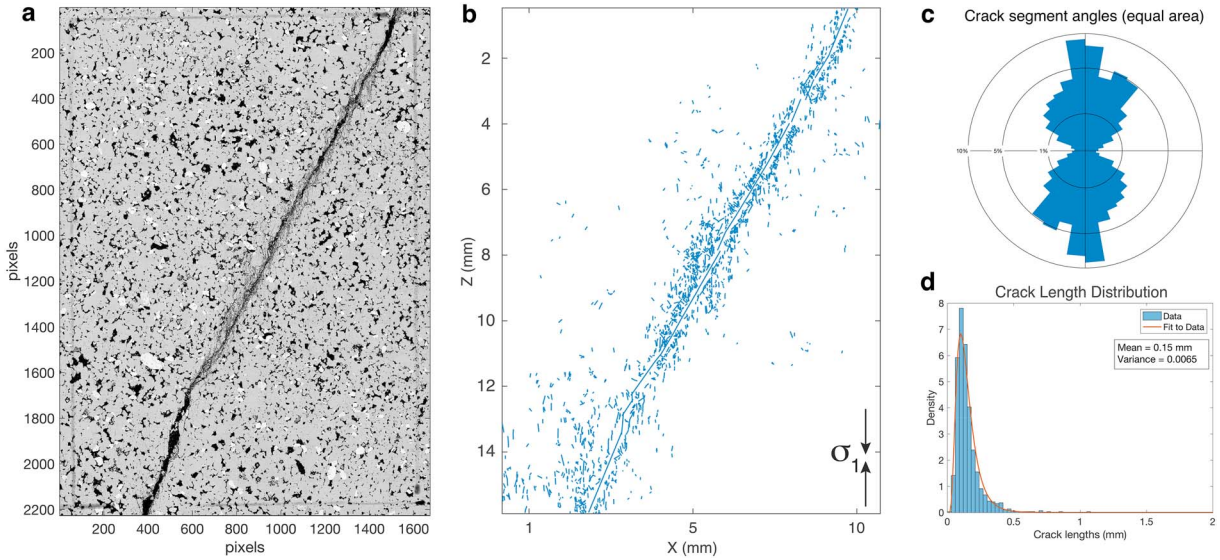

Figure 10. Fracture network in Sample 3. (a) Postfailure BSE high-resolution montage for Sample 3, deformed at P_{eff} of 30 MPa; σ_1 vertical. (b) Fracture map. (c) The inset shows rose diagram (equal area) of all the fracture segments. (d) Histogram of length distribution of cracks, after removing lines relative to shear fractures. The best fit (red curve) is a log-normal distribution, derived from MLE analysis, with an arithmetic mean of 0.15 mm and variance of 0.006.

Since we observed the onset of at least two orientation transitions—that is, between $a = 4$ to 8, and between $a = 16$ to 32—we further investigated the sample to identify the precise wavelet coefficients at which these transitions are detectable (Figure 7). In particular, we found that the first transition occurred between $a = 6$ and 7, corresponding to the clustering of initial tensile vertical cracks. The second abrupt change in orientation occurred between $a = 20$ and 22 corresponding to the propagation of the second and prominent shear plane.

3.2.2. Intermediate Effective Pressure—Sample 2

This sample was deformed at $P_{eff} = 15$ MPa ($P_c = 25$ MPa and $P_f = 10$ MPa; Figure 8). At the lowest resolution ($a = 4$), similar to the previous sample, the wavelet method detected the presence of diffuse and short subvertical cracks, aligned parallel to the direction of the maximum compressive stress. When lowering the resolution, for $a = 8$, we observed a shift in the crack orientation towards an inclined position (~26–28°). This transition marked the change in the fracture orientation to a macroscopic feature, corresponding to the time when the fault started to establish its position at an angle to the applied maximum compressive stress (vertical). At this scale, a minor set of conjugate fractures was also detected. Gradually (Figures 9c and 9d), the conjugate pattern became less resolvable ($a = 16$) and only the single major shear fracture appeared as a well-defined entity, with an average orientation of 26° ($a = 24$). As opposed to the previous sample (Sample 1), the minor conjugate cluster of cracks did not develop into a fully grown shear plane.

3.2.3. High Effective Pressure—Sample 3

This sample was deformed at P_{eff} of 30 MPa ($P_c = 40$ MPa and $P_f = 10$ MPa) and failure occurred along a single well-defined shear plane (Figure 10). First of all, to detect the initial emergence of small subvertical cracks we had to increase the resolution to $a = 2$ (Figure 10). These initial cracks were not diffused through the sample area but were all preferentially located along a relatively narrow zone (Figure 11). For $a = 4$ the wavelet already detected a single large cluster of cracks oblique (30°) to the applied maximum compressive stress. For increasing wavelet resolutions, we did not observe any further orientation transitions for either clusters of cracks nor for the final shear plane (Figure 11).

4. Discussion

The formation of a fault—a composite shear fracture—is a highly complex process involving the growth and the coalescence of small tensile cracks that are initially subparallel to the σ_1-axis (Dunn et al., 1973; Healy et al., 2006a; Lockner et al., 1991; Mandl, 2005; Reches & Lockner, 1994). High-resolution BSE images allowed us to study fault initiation over a significant area within samples deformed under a range of effective pressures (from 5 to 30 MPa; Figure 4).

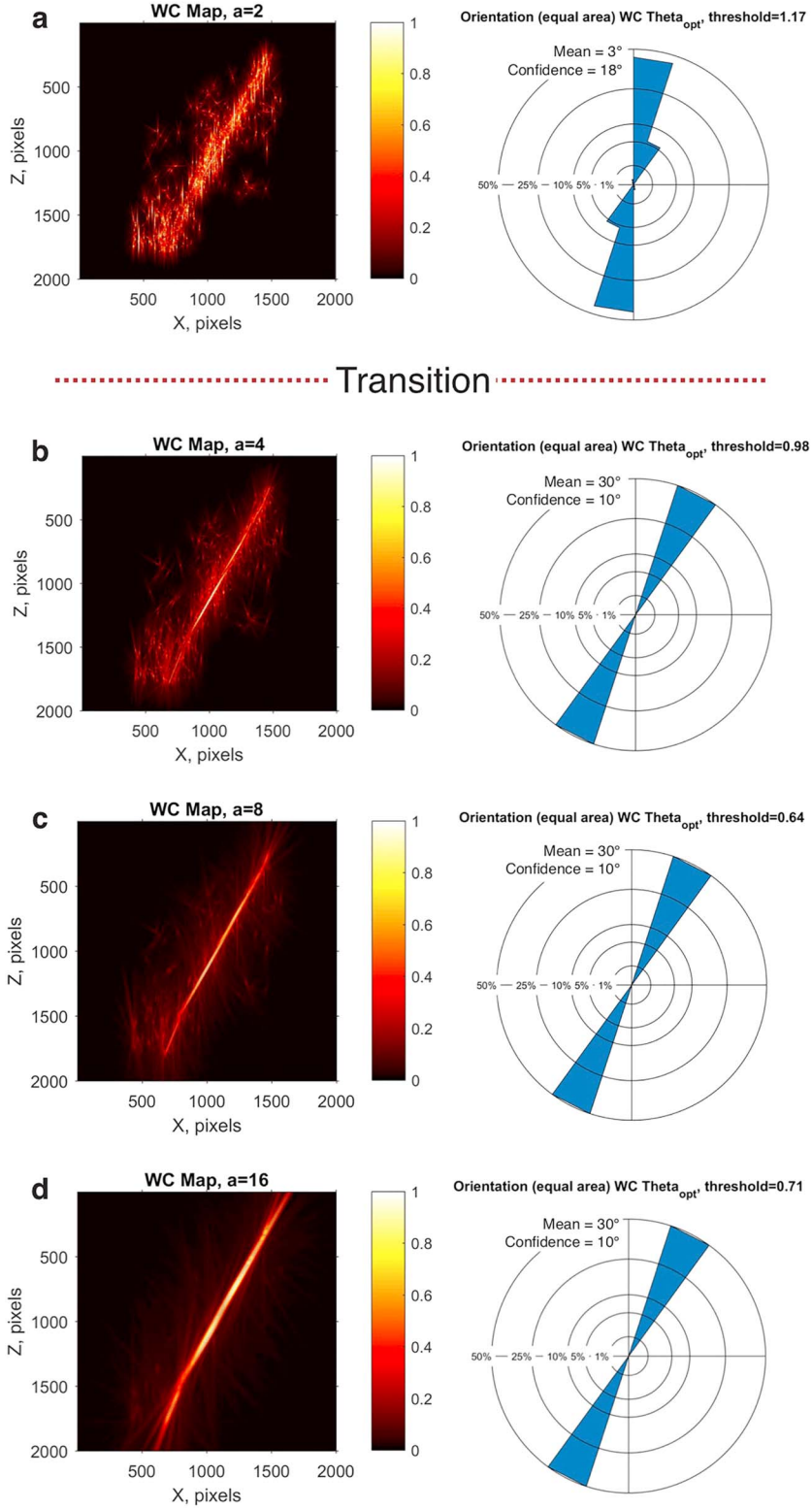

Figure 11. Morlet wavelet analysis applied to fracture network seen in Sample 3 (P_{eff} of 30 MPa). Color scale shows the values associated with normalized wavelet coefficients. Equal-area rose diagrams of fracture orientations correspond to wavelet coefficient (WC) maps at each filter resolution. Text boxes contain angular statistics: circular mean vector azimuth and angular confidence interval; σ_1 vertical.

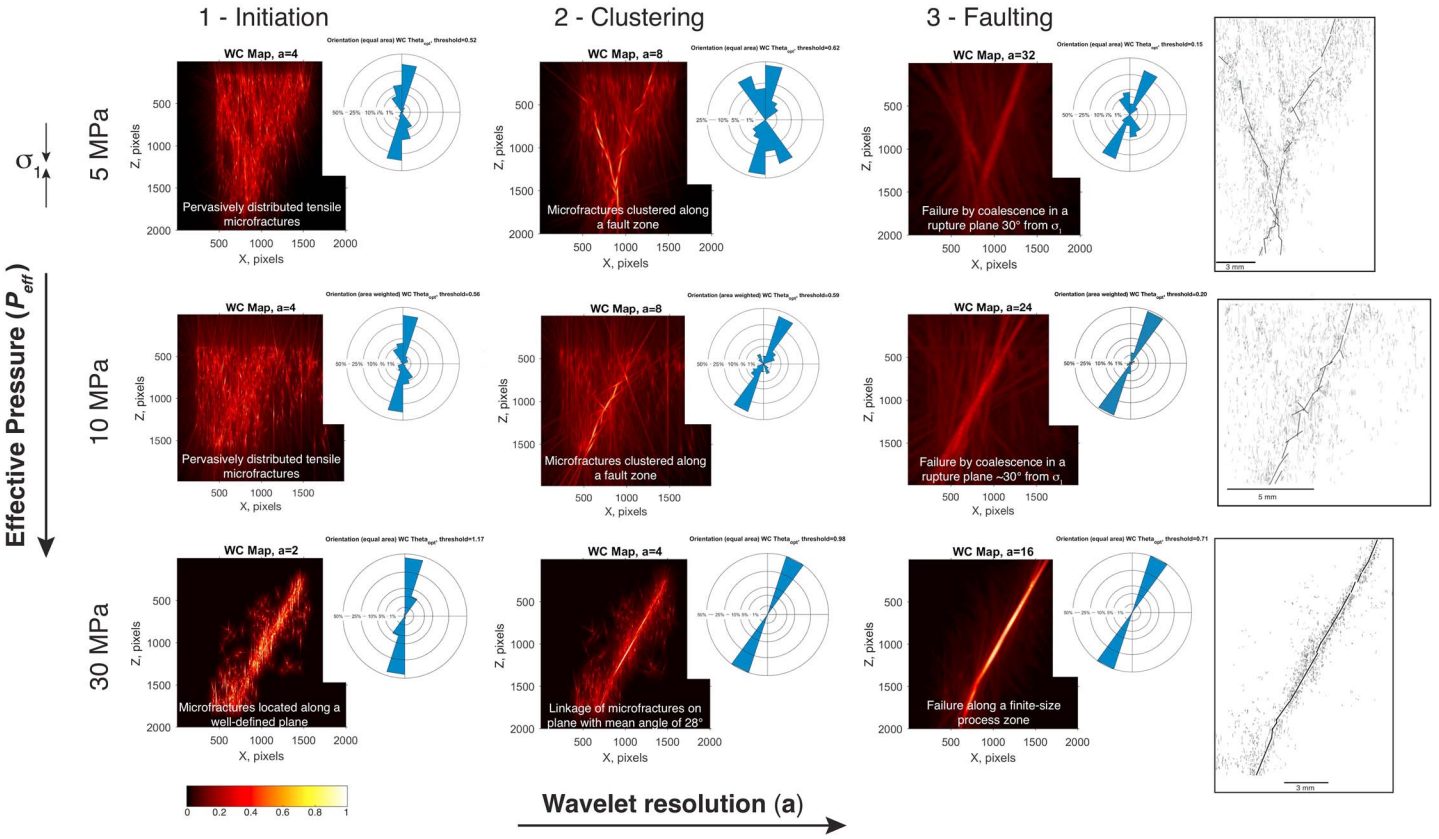

Figure 12. Overview of the difference observed in the deformation mechanism for increasing confining pressures as imaged with 2-D Morlet wavelets (resolution decreases rightward). The principal deformation stages (1 to 3) are represented by an early tensile cracking, clustering and interlinking of tensile cracks, and finally the formation of a defined shear plane. Similarities in the mode of fault development are observed for low (5 MPa) and intermediate (15 MPa) effective pressures: Pervasive tensile cracking initially affects the samples; subsequent interlinking reflects the formation crack clusters, which then coalesce to form the final shear plane. At relatively high effective pressure (30 MPa), cracks parallel to the applied main compressive stress (σ_1) mostly form along a well-developed plane; then rapid linkage localizes the fault along a finite-size process zone (Reches & Lockner, 1994; Renard et al., 2017).

Conceptually, wavelet coefficient maps for progressively lower resolutions ($1/a$) can be compared to a temporal sequence representing the deformation history of the sample, from the early tensile cracking, to crack interaction and eventual shear failure (Figure 12). The underlying assumption behind this "space for time" substitution in the analysis is that an intact rock transitions to bulk shear failure through the progressive nucleation, growth, interaction, and coalescence of tensile microcracks (Lockner et al., 1992). The fundamental difference seen via the wavelet analysis is that the evolution of crack sizes and orientation transitions between samples can be directly associated with the effect that effective pressure exerts on crack nucleation and propagation. It has been found (Mandl, 2005) that the growth of fractures is very sensitive to compressive stress normal to the crack planes. We therefore infer that shear fracturing becomes the dominant mechanism in two distinct ways in response to the loading conditions (Figure 12).

4.1. Low and Intermediate Effective Pressures

Based on our inferred temporal mapping of the wavelet analysis we observe that at low (5 MPa) and intermediate (15 MPa) effective pressures, the first features to form (a = 4) were pervasive short tensile cracks randomly located throughout the samples (Figure 6a). As time progresses (a = 8), the deformation reached a subsequent stage marked by the first orientation transition (Figure 5b). A previous analysis of the micromechanics of brittle failure in sandstones (Hazzard et al., 2000) showed that "secondary" cracking occurs along grain boundaries by shear rupturing of the cement at the contacts caused by rotation and slip of the grains under an applied load. The same mechanisms were seen by Dunn et al. (1973) as the crucial part of the process, because extension cracks unlock the ends of ready-to-fail grain-boundary cracks. For samples deformed at low and intermediate effective pressure, the application of a differential stress produced comminution and grain rotation until each grain is fixed by its neighbors. This mechanism determined the interlinking of the

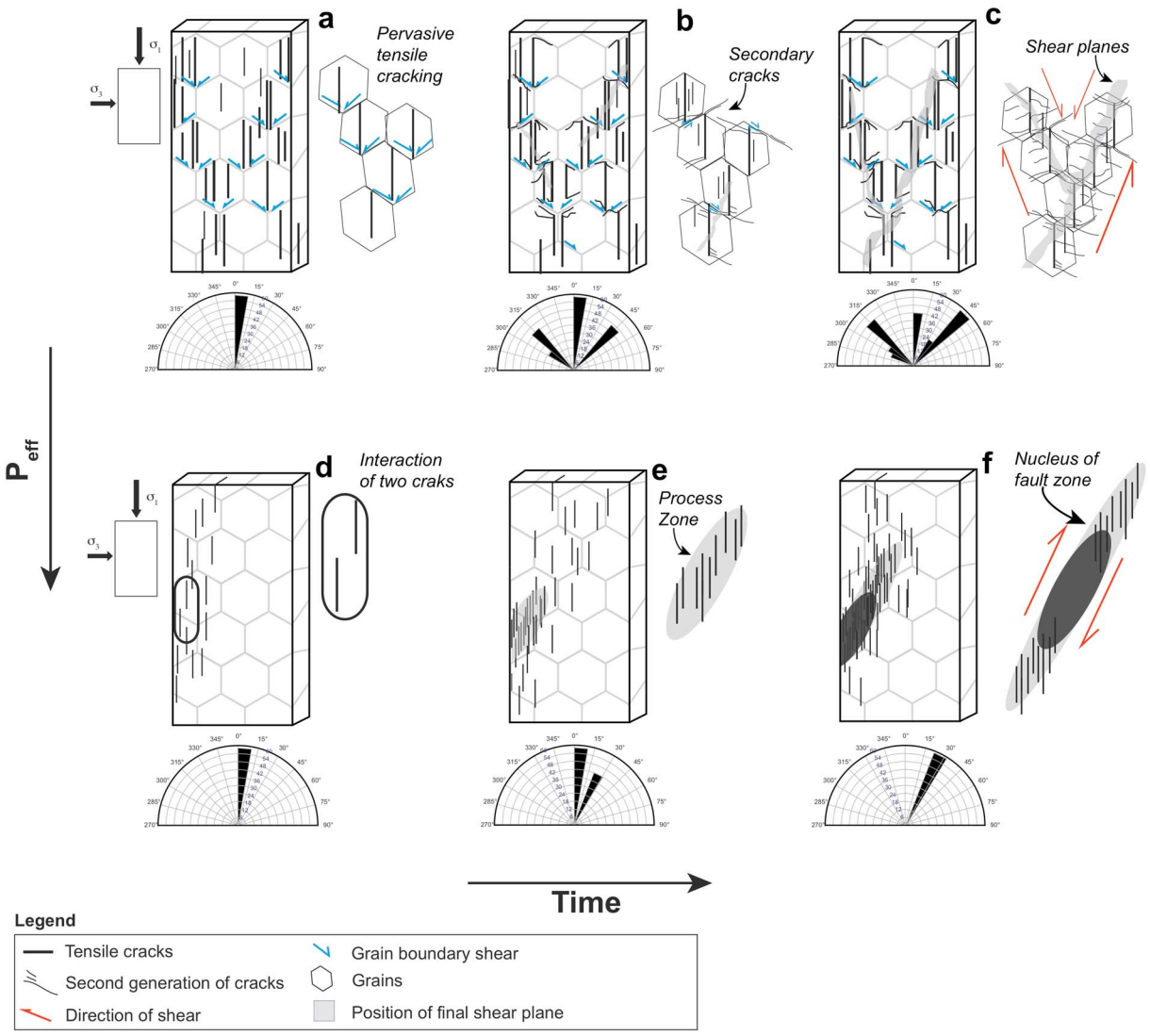

Figure 13. Schematic models for the two recognized shear initiation modes. The idealized samples (rectangular boxes) are under biaxial loading. The top images show the strain localization mode as seen at low (5 MPa) and intermediate (15 MPa) effective pressure. Deformation starts with pervasive tensile cracks parallel to the applied σ_1; it progresses with the growth of clusters of cracks, which, once reached a critical length and density, start interacting and coalescing to form the final shear planes. In the bottom images (modified after Reches & Lockner, 1994), at relatively high effective pressures (30 MPa), the deformation involves a rapid localization of strain, initiating with the interaction of short en-echelon tensile cracks, which then coalesce and give way to the propagation of the shear plane.

widespread axially (vertically) oriented small tensile cracks. When cracks became interlinked, we observed the formation of scattered clusters of cracks characterized by a different orientation—that is, different relative to the early tensile cracks—as apparent from wavelet coefficient maps and the number of petals in the corresponding rose diagrams (Figures 6 and 8). The distribution and the orientation of these clusters will influence the location of the final shear plane. On average, in both samples, the tensile fracture length is 0.24 mm (Figures 5d and 8d), which is comparable with the mean grain diameter of Hopeman Sandstone (Rizzo, Healy, Farrell, & Heap, 2017). Therefore, we infer that cracks tended to reach the edges of the grains before achieving sufficient interaction and coalescence (Katz & Reches, 2004). Further deformation in the samples caused clusters to expand and join, if favorably oriented, in a shear plane (a = 16, in Figures 6 and 9). Shear fractures then grew accumulating displacement during tensile cracking associated with deformation localizing on individual tensile crack and crack clusters (Figure 13).

A major effect of increasing the effective pressure from 5 to 15 MPa on the failure process is exemplified at the latest stage of deformation. For Sample 1, deformed at the lowest effective pressure (5 MPa), we observed the formation of two shear fractures with very irregular final profiles (Figures 6c and 6d), as shown by a wide range

of associated θ. On the other hand, for Sample 2, deformed at P_{eff} = 15 MPa, failure occurred along a more localized single plane, even though deformation initially produced similar effects in both samples—that is, randomly located diffuse tensile cracking.

Continuous macroscopic shear planes are therefore formed by the interlinking of axially oriented small-scale tensile cracks with oblique sliding cracks (along quartz grain-boundaries) with the same sense of right-lateral or left-lateral displacement (Figure 11). The described evolution takes place in a crack nucleation—rather than crack growth—dominated system culminating in a distributed deformation where the load is distributed through the numerous fractures. This model (Figure 12) also assumes that macroscopic shear planes formed due to interaction among many damage points (i.e., cluster of fractures), which formed prior to faulting (Katz & Reches, 2004; Renard et al., 2017, 2018).

4.2. High Effective Pressure

Similar considerations regarding our wavelet analysis as time lapse imaging of fault initiation can be applied to Sample 3 deformed at the highest effective pressure (30 MPa). The higher pressure caused the "early" development of the shear plane. This rapid localization did not allow tensile cracks to reach significant lengths; in fact, cracks are shorter on average (0.15 mm, Figure 10d). The cracks are therefore shorter than the average grain size in Hopeman sandstone. Furthermore, at half the wavelet scale (between $a = 2$ and $a = 4$, Figure 11), we observed that cracks had already achieved a density sufficient to promote interaction and coalescence compared to the previous specimens deformed at lower effective pressures. Overall, this process resulted in a very localized deformation, meaning that cracks formed simultaneously along a narrow-inclined zone (28° to the applied σ_1) where the shear plane eventually formed. Cracks were initially aligned parallel to σ_1 (a = 2), as seen for lower P_{eff}; we observed a single bulk transition in crack orientation ($a = 4$), after which no further changes occurred.

Reches and Lockner (1994) proposed that, for $P_c \geq 50$ MPa, faults grow in the wake of a process zone that is a finite size region of high stress concentration at fault tip in which the intact rock is disintegrated. In this model, tensile microfractures would be restricted to the fault vicinity and decay away from the fault. The failure model developed by Reches and Lockner (1994) predicts that the region of maximum stress induced by an opening tensile crack is inclined at an angle of at least 30° to the crack itself (and to the applied maximum compressive stress, σ_1). This angle exerts a fundamental control in the geometry of the final shear failure plane by promoting the en-echelon interaction of neighboring cracks (Healy et al., 2006b). High P_{eff} allows mechanical interaction predominantly between neighboring cracks which are in a favorable position, determining a specific cluster of en-echelon cracks to coalesce into a macrofracture only on one side of the crack-tip region; otherwise, the en-echelon ensemble would be stopped (Figure 12). This chain reaction causes the sample to fail by propagation of self-organized en-echelon cracks (Mandl, 2005).

4.3. Overall Implications and Applications of the Method

Our wavelet analysis proved useful for sharply distinguishing specific orientations at specific scales of observation, which would otherwise be lost in the complexity of a standard rose diagram containing all fracture trace orientations plotted for all scales simultaneously (e.g., compare Figures 4c and 5). The results obtained from our three initial samples suggest that, for relatively low effective pressures, cracks tend to form in large and diffuse clusters rather than uniformly along the fault zone, as seen for the highest P_{eff}. Furthermore, at relatively high effective pressure, cracks do not need to grow to the same lengths as for lower P_{eff}—that is, they do not scale with the sandstone grain size—to achieve interaction and coalescence (as summarized in Rizzo, Healy, Farrell, & Heap, 2017). This, in turn, results in the two different shear initiation modes observed through our wavelet analysis. Morlet wavelet analysis has detected that the inclination of the final shear plane, in all three samples, is in a range between 26° and 30° with respect to the maximum compression axis (Figures 5d, 8d, and 9d). Similar angular values were found both via experimental procedures (20–30° , Engelder, 1974; Reches & Lockner, 1994; Renard et al., 2018) and numerical models (26°, Healy et al., 2006a). We emphasize that our results are based on the assumption that all the mapped cracks were produced solely during the compression tests. More experiments and analyses on sandstones with different grain sizes are now required to further explore these findings. Further, we are yet to apply our technique to the process of compactant strain localization (i.e., the growth of compaction bands) in sandstones in the ductile regime (e.g., Baud et al., 2004; Heap et al., 2015).

Our initial application has been to a single rock type in an effort to reduce variables. However, the application of the described image processing technique to rock types with significant mineralogical or textural

heterogeneities might result in improved models for fracture coalescence. The methodology presented here can have important applications for recognizing larger length-scale mechanical heterogeneities controlling fault-scale rupture (e.g., Kim et al., 2004; Peacock, 2002) and fracture propagation during volcanic unrest (e.g., Gudmundsson, 2006; Kilburn & Voight, 1998; Kilburn, 2003). Just as a fault on the "small" scale of a laboratory sample localizes through extension and coalescence of microcracks, larger faults also grow by extension and coalescence of multiple segments (e.g., Cartwright et al., 1995). Rock failure is thus perceived as a multiscale process for which microscopic cracks can ultimately lead to macroscopic faulting. In addition, a variety of phenomena have been suggested as parameters that may be used for the prediction of faulting and the deformation and failure of a volcanic flank or dome, including temporal changes in strain, tilt, and creep. All these phenomena can be associated directly or indirectly with changes in the microcrack geometry.

5. Conclusions

An image processing method, namely, Morlet wavelet analysis, has been successful in exposing and quantifying the initiation and development of shear fracture formation in laboratory rock deformation tests. The analytical technique presented here has allowed us to detect the variations and abrupt transitions in orientation, length, and density occurring during the deformation, from early tensile cracking to the onset of a final shear fault. The ability of the Morlet wavelet to untangle the geometrical complexities proved straightforward due, for the most part, to its intrinsically anisotropic nature. Based on the derived wavelet coefficients maps obtained for three samples deformed at different effective pressures (5, 15, and 30 MPa), it was possible to derive conceptual models and infer possible mechanisms coupling the role of effective pressure to the localization of the shear plane. We show that, in the case of low and intermediate effective pressures (5 and 15 MPa, respectively), the wavelet analysis detects early tensile damage randomly distributed throughout the samples. An abrupt change in crack orientation corresponds to the start of crack interaction to form clusters, with the detected critical crack length comparable with the average grain size of the samples (0.24 mm). Further transitions in crack orientation occur as the result of a localization of the shear plane, which eventually causes the sample to fail. In contrast, for our highest effective pressure (30 MPa), wavelet analysis detects early vertical tensile cracking occurring along a narrow-inclined zone. Cracks do not need to reach the grain edges to achieve interaction due to their relatively high density, but subsequent deformation suddenly localizes, as identified by the single bulk transition of crack orientations. Thus, the results of this study show how variations in the applied stress field (i.e., effective pressure) on the same material play a significant role in controlling the mechanism of initiation and development of shear fracture.

Acknowledgments
We thank David Wilde and Peter Greatbatch at Keele University for careful thin section preparation. We are thankful to Peter Chung at Glasgow for acquiring the SEM BSE images, and Thierry Reuschlé for the maintenance of the triaxial press at Strasbourg. This work forms part of the NERC grant "Anisotropy of permeability" for David Healy (NE/N003063/1), which is gratefully acknowledged. We thank Tom Mitchell for his feedback on an early version of the manuscript. The authors would like to thank Douglas Schmitt, Alain Plattner, Beatriz Menéndez, and Philip Benson for their comments that helped clarify several aspects of the manuscript. The codes for the wavelet analysis used in this study are available on GitHub as a complementary tool in FracPaQ (https://github.com/DaveHealy-Aberdeen/FracPaQ); the SEM-BSE images of the thin sections are available from Figshare: 10.6084/m9.figshare.7140290.

References

Antoine, J.-P., Carrette, P., Murenzi, R., & Piette, B. (1993). Image analysis with two-dimensional continuous wavelet transform. *Signal Processing*, *31*(3), 241–272. https://doi.org/10.1016/0165-1684(93)90085-O

Arena, A., Delle Piane, C., & Sarout, J. (2014). A new computational approach to cracks quantification from 2D image analysis: Application to micro-cracks description in rocks. *Computer and Geosciences*, *66*, 106–120. https://doi.org/10.1016/j.cageo.2014.01.007

Baud, P., Klein, E., & Wong, T.-F. (2004). Compaction localization in porous sandstones: Spatial evolution of damage and acoustic emission activity. *Journal of Structural Geology*, *26*(4), 603–624. https://doi.org/10.1016/j.jsg.2003.09.002

Baud, P., Zhu, W., & Wong, T.-F (2000). Failure mode and weaking effect of water on sandstone. *Journal of Geophysical Research*, *105*(B7), 16,371–16,389. https://doi.org/10.1029/2000JB900087

Cartwright, J. A., Trudgill, B. D., & Mansfield, C. S. (1995). Fault growth by segment linkage: an explanation for scatter in maximum displacement and trace length data from the Canyonlands Grabens of SE Utah. *Journal of Structural Geology*, *17*(9), 1319–1326. https://doi.org/10.1016/0191-8141(95)00033-A

Darrozes, J., Gaillot, P., De Saint-Blanquat, M., & Bouchez, J. L. (1997). Software for multi-scale image analysis: The normalized optimized anisotropic wavelet coefficient method. *Computers and Geosciences*, *23*(8), 889–895. https://doi.org/10.1016/S0098-3004(97)00063-0

Delle Piane, C., Arena, A., Sarout, J., Esteban, L., & Cazes, E. (2015). Micro-crack enhanced permeability in tight rocks: An experimental and microstructural study. *Tectonophysics*, *665*, 149–156. https://doi.org/10.1016/j.tecto.2015.10.001

Dunn, D. E., LaFountain, L. J., & Jackson, R. E. (1973). Porosity dependence and mechanism of brittle fracture in sandstones. *Journal of Geophysical Research*, *78*(14), 2403–2417. https://doi.org/10.1029/JB078i014p02403

Edwards, H. E., Becker, A. D., & Howell, J. A. (1993). Compartmentalization of an aeolian sandstone by structural heterogeneities: Permo-triassic Hopeman Sandstone, Moray Firth, Scotland. *Geological Society*, *73*(1), 339–365. https://doi.org/10.1144/GSL.SP.1993.073.01.20

Engelder, J. T. (1974). Cataclasis and the Generation of Fault Gouge. *GSA Bulletin*, *85*(10), 1515–1522. https://doi.org/10.1130/0016-7606(1974)85<1515:CATGOF>2.0.CO;2

Farquharson, J. I., Baud, P., & Heap, M. J. (2017). Inelastic compaction and permeability evolution in volcanic rock. *Solid Earth*, *8*(2), 561–581. https://doi.org/10.5194/se-8-561-2017

Farrell, N. J. C., & Healy, D. (2017). Anisotropic pore fabrics in faulted porous sandstones. *Journal of Structural Geology*, *104*, 125–141. https://doi.org/10.1016/j.jsg.2017.09.010

Farrell, N. J. C., Healy, D., & Taylor, C. (2014). Anisotropy of Permeability in Faulted Porous Sandstones. *Journal of Structural Geology*, *63*, 50–67. https://doi.org/10.1016/j.jsg.2014.02.008

Gaillot, P., Darrozes, J., & Bouchez, J. L. (1999). Wavelet transform: a future of rock fabric analysis? *Journal of Structural Geology*, *21*(11), 1615–1621. https://doi.org/10.1016/S0191-8141(99)00073-5

Gaillot, P., Darrozes, J., Courjault-Radé, P., & Amorese, D. (2002). Structural analysis of hypocentral distribution of an earthquake sequence using anisotropic wavelets: Method and application. *Journal of Geophysical Research*, *107*(B10), 2218. https://doi.org/10.1029/2001JB000212

Gaillot, P., Darrozes, J., De, Blanquat, Saint, M., & Ouillon, G. (1997). The normalised-optimised anisotropic wavelet coefficient (NOAWC) method: an image processing tool for multi-scale analysis of rock fabric. *Geophysical Research Letters*, *24*(14), 1819–1822. https://doi.org/10.1029/97GL01601

Griffiths, L., Heap, M. J., Baud, P., & Schmittbuhl, J. (2017). Quantification of microcrack characteristics and implications for stiffness and strength of granite. *International Journal of Rock Mechanics and Mining Sciences*, *100*, 138–150. https://doi.org/10.1016/j.ijrmms.2017.10.013

Gudmundsson, A. (2006). How local stresses control magma-chamber ruptures, dyke injections, and eruptions in composite volcanoes. *Earth-Science Reviews*, *79*(1-2), 1–31. https://doi.org/10.1016/j.earscirev.2006.06.006

Hazzard, J. F., Young, R. P., & Maxwell, S. C. (2000). Micromechanical modeling of cracking and failure in brittle rocks. *Journal of Geophysical Research*, *105*(B7), 16,683–16,697. https://doi.org/10.1029/2000JB900085

Healy, D., Jones, R. R., & Holdsworth, R. E. (2006a). New insights into the development of brittle shear fractures from a 3-D numerical model of microcrack interaction. *Earth and Planetary Science Letters*, *249*(1-2), 14–28. https://doi.org/10.1016/j.epsl.2006.06.041

Healy, D., Jones, R. R., & Holdsworth, R. E. (2006b). Three-dimensional brittle shear fracturing by tensile crack interaction. *Nature*, *439*(7072), 64–7. https://doi.org/10.1038/nature04346

Healy, D., Rizzo, R. E., Cornwell, D. G., Farrell, N. J. C., Watkins, H., Timms, N. E., et al. (2017). Fracpaq: A MATLAB^{TM} toolbox for the quantification of fracture patterns. *Journal of Structural Geology*, *95*, 1–16. https://doi.org/10.1016/j.jsg.2016.12.003

Heap, M. J., Brantut, N., Baud, P., & Meredith, P. G. (2015). Time-dependent compaction band formation in sandstone. *Journal of Geophysical Research: Solid Earth*, *120*, 4808–4830. https://doi.org/10.1002/2015JB012022

Heap, M. J., & Wadsworth, F. B. (2016). Closing an open system: pore pressure changes in permeable edifice rock at high strain rates. *Journal of Volcanology and Geothermal Research*, *315*, 40–50. https://doi.org/10.1016/j.jvolgeores.2016.02.011

Jourde, H., Flodin, E. A., Aydin, A., Durlofsky, L. J., & Wen, X. (2002). Computing permeability of fault zones in eolian sandstone from outcrop measurements. *AAPG Bulletin*, *86*(7), 1187–1200.

Katz, O., & Reches, Z. (2004). Microfracturing, damage, and failure of brittle granites. *Journal of Geophysical Research*, *109*, B01206. https://doi.org/10.1029/2002JB001961

Kilburn, C. R. J. (2003). Multiscale fracturing as a key to forecasting volcanic eruptions. *Journal of Volcanology and Geothermal Research*, *125*(3), 271–289. https://doi.org/10.1016/S0377-0273(03)00117-3

Kilburn, C. R. J., & Voight, B. (1998). Slow rock fracture as eruption precursor at Soufriere Hills Volcano, Montserrat. *Geophysical Research Letters*, *25*(19), 3665–3668. https://doi.org/10.1029/98GL01609

Kim, Y. S., Peacock, D. C. P., & Sanderson, D. J. (2004). Fault damage zones. *Journal of Structural Geology*, *26*, 503–517. https://doi.org/10.1016/j.jsg.2003.08.002

Klein, E., Baud, P., Reuschlé, T., & Wong, T. F. (2001). Mechanical behaviour and failure mode of Bentheim sandstone under triaxial compression. *Physics and Chemistry of the Earth Part A*, *26*(1-2), 21–25. https://doi.org/10.1016/S1464-1895(01)00017-5

Lockner, D. A. (1993). The role of acoustic emission in the study of rock fracture. *International Journal of Rock Mechanics and Mining Sciences and Geomechanics Abstracts*, *30*(7), 883–899. https://doi.org/10.1016/0148-9062(93)90041-B

Lockner, D. A., Byerlee, J. D., Kuksenko, V., Ponomarev, A., & Sidorin, A. (1991). Quasi-static fault growth and shear fracture energy in granite. *Nature*, *350*(6313), 39–42.

Lockner, D. A., Reches, Z. E., & Moore, D. E. (1992). Microcrack interaction leading to shear fracture. In *Rock Mechanics, Proceedings of the 33rd U.S. Symposium* (pp. 807–816).

Mandl, G. (2005). *Rock Joints, The Mechanical Genesis*. Berlin: Springer.

McGrath, A. G., & Davison, I. (1995). Damage zone geometry around fault tips. *Journal of Structural Geology*, *17*(7), 1011–1024. https://doi.org/10.1016/0191-8141(94)00116-H

Menendez, B., Zhu, W., & Wong, T. (1996). Micromechanics of brittle faulting and cataclastic flow in Berea sandstone. *Journal of Structural Geology*, *18*(1), 1–16. https://doi.org/10.1016/0191-8141(95)00076-P

Moore, D. E., & Lockner, D. A. (1995). The role of microcracking in shear-fracture propagation in granite. *Journal of Structural Geology*, *17*(1), 95–114. https://doi.org/10.1016/0191-8141(94)E0018-T

Neupauer, R. M., & Powell, K. L. (2005). A fully-anisotropic Morlet wavelet to identify dominant orientations in a porous medium. *Computers and Geosciences*, *31*(4), 465–471. https://doi.org/10.1016/j.cageo.2004.10.014

Ouillon, G., Castaing, C., & Sornette, D. (1996). Hierarchical geometry of faulting. *Journal of Geophysical Research*, *101*(B3), 5477–5487. https://doi.org/10.1029/95JB02242

Ouillon, G., Sornette, D., & Castaing, C. (1995). Organisation of joints and faults from 1-cm to 100-km scales revealed by optimized anisotropic wavelet coefficient method and multifractal analysis. *Nonlinear Processes in Geophysics*, *2*, 158–177. https://doi.org/10.5194/npg-2-158-1995

Peacock, D. C. (2002). Propagation, interaction and linkage in normal fault systems. *Earth-Science Reviews*, *58*(1-2), 121–142. https://doi.org/10.1016/S0012-8252(01)00085-X

Petit, J. P., & Barquins, M. (1988). Can natural faults propagate under Mode II conditions? *Tectonics*, *7*(6), 1243–1256. https://doi.org/10.1029/TC007i006p01243

Reches, Z. E., & Lockner, D. A. (1994). Nucleation and growth of faults in brittle rocks. *Journal of Geophysical Research*, *99*(B9), 18,159–18,173. https://doi.org/10.1029/94JB00115

Reedy, C. L. (2006). Review of digital image analysis of petrographic thin sections in conservation research. *Journal of the American Institute of Conservation*, *45*(2), 127–146. https://doi.org/10.1179/019713606806112531

Renard, F., Cordonnier, B., Kobchenko, M., Kandula, N., Weiss, J., & Zhu, W. (2017). Microscale characterization of rupture nucleation unravels precursors to faulting in rocks. *Earth and Planetary Science Letters*, *476*, 69–78. https://doi.org/10.1016/j.epsl.2017.08.002

Renard, F., Weiss, J., Mathiesen, J., Ben-Zion, Y., Kandula, N., & Cordonnier, B. (2018). Critical evolution of damage toward system-size failure in crystalline rock. *Journal of Geophysical Research: Solid Earth*, *123*, 1969–1986. https://doi.org/10.1002/2017JB014964

Rizzo, R. E., Healy, D., & De Siena, L. (2017). Benefits of maximum likelihood estimators for fracture attribute analysis: Implications for permeability and up-scaling. *Journal of Structural Geology*, *95*, 17–31. https://doi.org/10.1016/j.jsg.2016.12.005

Rizzo, R. E., Healy, D., Farrell, N. J., & Heap, M. J. (2017). Riding the right wavelet: Quantifying scale transitions in fractured rocks. *Geophysical Research Letters*, *44*, 11,808–11,815. https://doi.org/10.1002/2017GL075784

Stanchits, S., Vinciguerra, S., & Dresen, G. (2006). Ultrasonic velocities, acoustic emission characteristics and crack damage of basalt and granite. *Pure and Applied Geophysics*, *163*(5-6), 974–993. https://doi.org/10.1007/s00024-006-0059-5

Vasseur, J., Wadsworth, F. B., Heap, M. J., Main, I. G., Lavallée, Y., & Dingwell, D. B. (2017). Does an inter-flaw length control the accuracy of rupture forecasting in geological materials? *Earth and Planetary Science Letters*, *475*, 181–189. https://doi.org/10.1016/j.epsl.2017.07.011

Voorn, M., Exner, U., & Rath, A. (2013). Multiscale Hessian fracture filtering for the enhancement and segmentation of narrow fracture in 3D image data. *Computers and Geosciences*, *57*, 44–53. https://doi.org/10.1016/j.cageo.2013.03.006

Wibberley, C. A. J., Petit, J. P., & Rives, T. (2000). Micromechanics of shear rupture and the control of normal stress. *Journal of Structural Geology*, *22*(4), 411–427. https://doi.org/10.1016/S0191-8141(99)00158-3

Wong, T.-F., David, C., & Zhu, W. (1997). The transition from brittle faulting to cataclasic flow in porous sandstones: Mechanical deformation. *Journal of Geophysical Research*, *102*(B2), 3009–3025. https://doi.org/10.1029/96JB03282

Yeum, C. M., & Dyke, S. J. (2015). Vision-based automated crack detection for bridge inspection. *Computer-Aided Civil and Infrastructure Engineering*, *30*, 759–770. https://doi.org/10.1111/mice.12141